

# Construction of Hierarchical Surface on Carbon Fiber Paper for Lithium Metal Batteries with Superior Stability

Youn-Ki Lee, Ki-Yeop Cho, Sora Lee, Jiho Choi, Gwanwon Lee, Han-Ik Joh, KwangSup Eom,\* and Sungho Lee\*

Lithium is perceived as an ideal anode for next generation batteries with high-energy density. However, the critical issue of the intractable growth of Li dendrites, which leads to a poor cycling life, still remains. Herein, a hierarchical surface is designed and constructed on carbon fiber (CF) using binders in fabricated CF paper (CFP). The lightweight CF with high mechanical properties is facilitated to establish a 3D network structure as an alternative to Cu foil. The binders are transformed into oxygen-containing amorphous carbon and sodium carbonate ( $\text{Na}_2\text{CO}_3$ ) using a low-temperature carbonization process, leading to uniform Li nucleation and a stable solid electrolyte interphase layer with inorganic components. In the electrochemical test, the CFP with amorphous carbon and  $\text{Na}_2\text{CO}_3$  (ANCFP) shows a low Li nucleation overpotential and smooth dendrite-free Li plating. Furthermore, the ANCFP electrode exhibits good cycling stability in half and symmetrical cells. A full-cell assembled using a  $\text{LiFePO}_4$  cathode with high loading ( $\approx 13 \text{ mg cm}^{-2}$ ) achieves a high-energy density of  $428 \text{ Wh kg}^{-1}$  (at  $0.1 \text{ C}$ ) and an excellent capacity retention of  $85\%$  at  $1 \text{ C}$  after 300 cycles. This strategy is expected to help realize highly stable Li metal anodes for practical application by suppressing Li dendrite growth.

## 1. Introduction

The demand for rechargeable batteries has increased owing to the global trend of utilizing electric vehicles (EVs) instead of gasoline and diesel vehicles to achieve net-zero carbon dioxide ( $\text{CO}_2$ ) emissions, so-called “carbon-neutral.”<sup>[1,2]</sup> In particular, lithium-ion batteries (LiBs) are receiving the most attention due to their high energy density and long-term stability. Nevertheless, the energy density of the presently commercialized LiBs has not satisfied the requirements for the rapidly growing EV industry. Hence, alternative electrode materials with significantly higher energy density for both the anode and cathode are being explored. Accordingly, Li metal anode (LMA) is the most promising candidate due to its high specific ( $3860 \text{ mAh g}^{-1}$ ) and volumetric capacities ( $2061 \text{ mAh cm}^{-3}$ ), and low electrode potential ( $-3.04 \text{ V}$  vs standard hydrogen

electrode (SHE)), which greatly increase the energy density of batteries.<sup>[3–6]</sup> When using the LMA, however, the inevitable growth of Li dendrites occurs during the electrochemical Li plating/stripping process, resulting in short circuiting, dead Li, and low coulombic efficiency (CE), leading to a battery poor lifespan.<sup>[7–9]</sup> In particular, the initial formation of problematic Li dendrites is dominated by the localized distribution of current density, Li-ion concentration in the electrolyte, and Li-ion transport according to the Sand's time equation.<sup>[10,11]</sup> The dendrites preferably grow on the non-uniform surface of the substrate, which has both favorable and unfavorable nucleation sites, because Li growth preferentially occurs on sites where Li has already nucleated.<sup>[8,12,13]</sup> Moreover, the electrolyte consumption at the morphologically changing Li surface results in the additional formation of a solid electrolyte interphase (SEI) layer. Hence, numerous studies have focused on the development of effective strategies for suppressing Li dendrites, such as introducing an artificial SEI, designing dendrite-inhibiting electrolytes, modifying the interface with high lithiophilicity, providing three-dimensional (3D) conductive support, and regulating the membrane structure.<sup>[14–21]</sup>


A recent problem-solving strategy involves the modification of current collectors (CCs) by constructing a porous and nano-structured 3D framework, and has been widely studied using metal, non-metal, and their hybrid-based materials.<sup>[22–24]</sup> 3D architectures on CCs provide high surface area, effective

Y.-K. Lee, S. Lee, J. Choi, G. Lee, S. Lee  
Carbon Composite Materials Research Center  
Korea Institute of Science and Technology (KIST)  
92 Chundong-ro, Bongdong-eup, Wanju-gun,  
Jeollabuk-do 55324, Republic of Korea  
E-mail: sunghol@kist.re.kr

Y.-K. Lee, K.-Y. Cho, K. Eom  
School of Materials Science and Engineering  
Gwangju Institute of Science and Technology (GIST)  
123 Cheomdangwagi-ro, Buk-gu, Gwangju 61005, Republic of Korea  
E-mail: keom@gist.ac.kr

G. Lee, H.-I. Joh  
Department of Energy Engineering  
Konkuk University  
120 Neungdong-ro, Gwangjin-gu, Seoul 05029, Republic of Korea  
S. Lee

Department of Quantum System Engineering  
Jeonbuk National University  
567 Baekje-ro, Deokjin-gu, Jeonju-si, Jeonbuk 54896, Republic of Korea

 The ORCID identification number(s) for the author(s) of this article can be found under <https://doi.org/10.1002/aenm.202203770>.

© 2023 The Authors. Advanced Energy Materials published by Wiley-VCH GmbH. This is an open access article under the terms of the Creative Commons Attribution-NonCommercial-NoDerivs License, which permits use and distribution in any medium, provided the original work is properly cited, the use is non-commercial and no modifications or adaptations are made.

DOI: 10.1002/aenm.202203770

Li-ion diffusion, and large internal space, leading to the inhibition of Li dendrites and sufficient accommodation for Li storage. Using carbon-based CCs as an alternative to metal-based CCs can be a significantly more effective solution for Li metal batteries (LMBs) with high gravimetric energy density and their commercialization due to its unique advantages of light weight and cheap precursor.<sup>[25–27]</sup> However, Li deposition on its surface is unfavorable as carbon-based materials intrinsically exhibit a lithiophobic nature.<sup>[28–30]</sup> Interfacial engineering on carbon-based materials is therefore required to improve its affinity with Li metal, and some related studies have been reported. For instance, the chemical and structural modification on a carbon skeleton yielded excellent lithiophilicity by the adjustment of electronegativity, Li adsorption, local dipole, and charge transfer.<sup>[31–33]</sup> Consequently, the carbon materials with hetero-atom doping and defect sites exhibited uniform Li nucleation.<sup>[34,35]</sup> Unfortunately, the chemical and structural defect sites negatively influence the SEI layer.<sup>[36]</sup> Although an ideal SEI layer with high mechanical strength contributes to the protection layer for the suppression of Li dendrites,<sup>[37–40]</sup> these defects serve to boost the additional reduction of the electrolyte, resulting in an undesirable SEI layer.<sup>[36]</sup> Therefore, it is necessary to provide a state-of-the-art LMA which possesses lithiophilic sites as well as a stable SEI layer on the carbon-based electrode for high-performance batteries. In particular, the facile interfacial modification of carbon-based materials could be one of the strategies for practically realizing LMAs.

In this context, this study introduces the construction of a hierarchical surface on commercial carbon fibers (CFs) using carbonized binders to simultaneously build a lithiophilic site and stable SEI layer. Specifically, CF paper (CFP) was employed to prepare a 3D free-standing LMA. Polyacrylic acid (PAA) and sodium carboxymethyl cellulose (Na-CMC) binders were used in the fabrication of CFP to simultaneously ensure the uniform dispersion of CF and mechanical strength of the fabricated CFP. Since polymers can be easily transformed into carbon materials with hetero-atoms by pyrolysis,<sup>[41,42]</sup> amorphous carbon structures with lithiophilic oxygen functional groups can be formed by the dissociation and rearrangement of polymer chains of

PAA and Na-CMC using low-temperature carbonization. Additionally, the sodium carbonate ( $\text{Na}_2\text{CO}_3$ ) resulting from the decomposition of the polymer chains and Na salt in Na-CMC is known to be good compounds for forming a stable SEI layer, which can lead to the enhanced electrochemical performance of Li-based battery system, as previously reported.<sup>[43–45]</sup> In summary, the proposed strategy for constructing a hierarchical surface on the CF using oxygen-containing amorphous carbon and  $\text{Na}_2\text{CO}_3$  is expected to benefit from the following advantages, namely (1) CF is an adequate candidate for LMA as an alternative to Cu foil because of its low density, high mechanical properties, strong chemical resistance, good electrical conductivity, and 3D structural framework; (2) the oxygen-containing amorphous carbon acts as lithiophilic Li nucleation sites, promoting uniform Li plating on the entire CF surface; and (3) the  $\text{Na}_2\text{CO}_3$  can attract bis(trifluoromethanesulfonyl)imide (TFSI<sup>−</sup>) anions to the reactive surface, contributing to the formation of an inorganic-rich SEI layer with high chemical/mechanical stability. Consequently, the modified CFP with oxygen-containing amorphous carbon and  $\text{Na}_2\text{CO}_3$  (ANCFP) exhibited greater stability and higher energy density even in high-loading cathode ( $\approx 2$  mAh) full cells.

## 2. Results and Discussion

### 2.1. Characterizations of ANCFP

To effectively suppress Li dendrites on carbon-based materials with lithiophobicity, interfacial modification is necessary for enhancing their Li affinity. Further, the formation of protection layer on the surface (i.e., inorganic-rich SEI layer) also alleviates Li dendrites owing to high mechanical strength. Therefore, constructing a lithiophilic site and stable SEI layer on the CF surface is required to prevent the Li dendritic growth. **Figure 1** presents a schematic showing our strategy for constructing CFP with hierarchical surfaces for a stable Li electroplating behavior. ANCFP, CFP comprising amorphous carbon and  $\text{Na}_2\text{CO}_3$  on the surface, was fabricated by carbonizing pristine

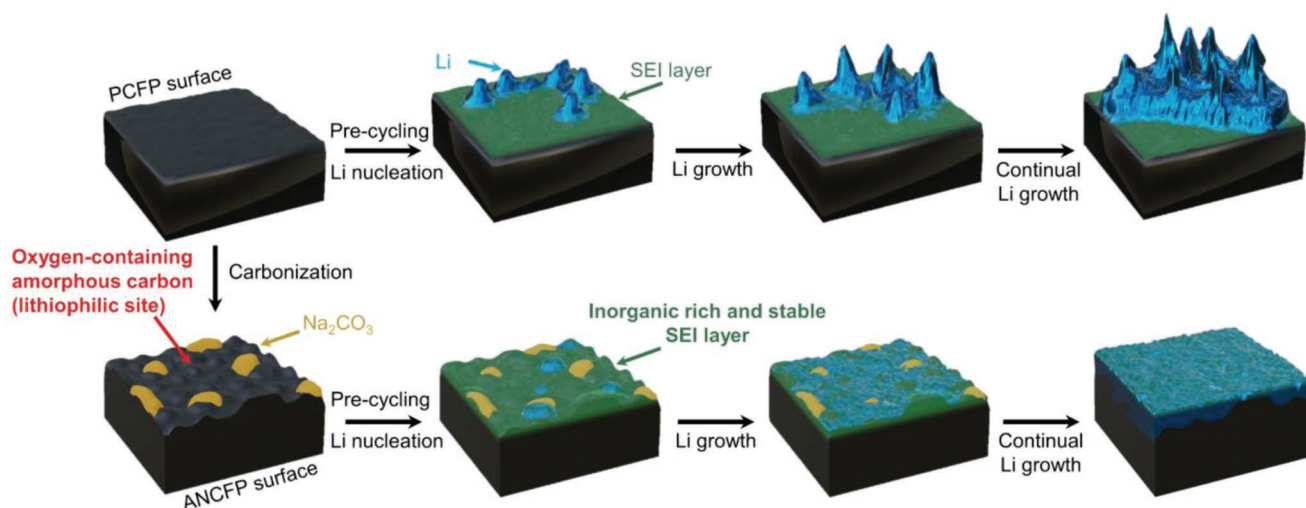


**Figure 1.** Schematic illustration of the Li nucleation and growth behaviors on PCFP and ANCFP.

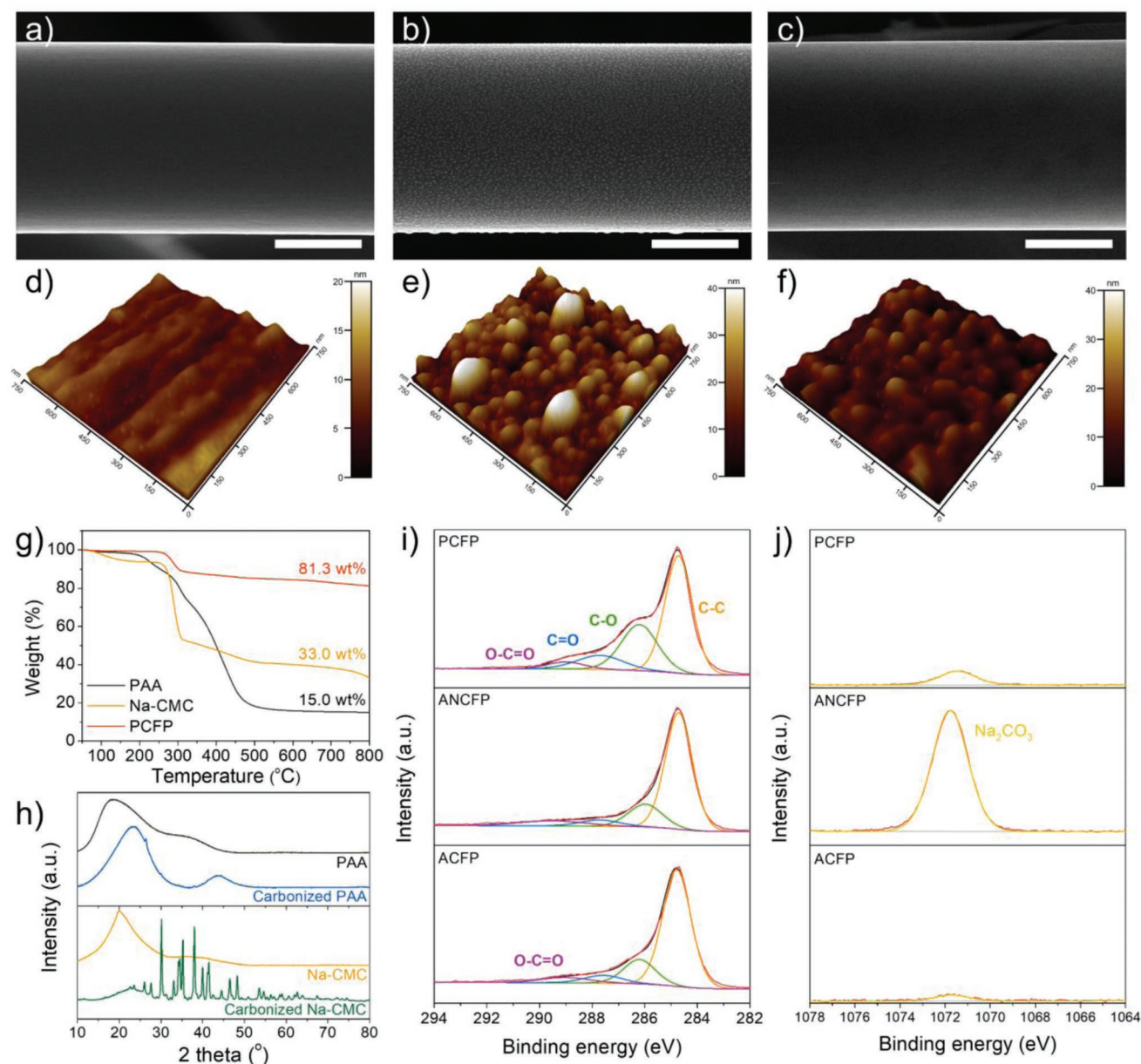


**Figure 2.** SEM micrographs (scale: 3 μm) and AFM images (0.75 × 0.75 μm) of a,d) PCFP, b,e) ANCFP, and c,f) ACFP. g) TGA thermograms of PAA, CMC, and PCFP under an inert atmosphere. h) XRD patterns of PAA and Na-CMC before and after carbonization. XPS i) C1s and j) Na1s spectra of PCFP, ANCFP, and ACFP.

CFP (PCFP) with PAA and Na-CMC binders at 800 °C. In particular, the  $\text{Na}_2\text{CO}_3$  formed on the CF surface can preferentially decompose the  $\text{TFSI}^-$  anions to form an inorganic-rich surface layer during the initial Li deposition/stripping cycles. Since the inorganic-rich surface layer has a high mechanical strength and low Li-ion diffusion barrier, it can improve the stability during Li deposition/stripping. Moreover, the entirely covered oxygen-containing amorphous carbon on the CF surface will guide the uniform Li electroplating by creating a lithophilic surface, as shown in the schematic. In contrast, PCFP will lead to uneven Li nucleation on the surface because of its lithiophobic nature. With continuous Li electroplating, ANCFP will facilitate homogeneous Li growth due to the lithophilic site and inorganic-rich

SEI layer, whereas PCFP promotes the dendritic formation of Li. Hence, we believe that ANCFP can simultaneously ensure high lithophilicity and a highly stable SEI layer on the CF surface, which are known to be the most crucial characteristics for developing a highly stable LMA.

To realize the aforementioned strategy, three types of CFPs were prepared to systematically investigate the effect of oxygen-containing amorphous carbon and  $\text{Na}_2\text{CO}_3$  on the CF surface, namely, PCFP (before carbonization), ANCFP (after carbonization), and CFP with amorphous carbon (ACFP, washed ANCFP using deionized (DI) water). First, the morphologies of the PCFP, ANCFP, and ACFP samples were characterized. Figure 2a and Figure S1a (Supporting Information) show that



the chopped CFs with a neat surface before carbonization were entangled with binders. In contrast, carbonization at 800 °C induced morphological changes in which nano-sized particles were present on the surface of the CFs with a retaining paper framework (Figure 2b and Figure S2b, Supporting Information). The nano-sized particles on the CF surface disappeared after ANCFP was washed with DI water (Figure 2c and Figure S2c, Supporting Information). The detailed morphological changes were clearly confirmed by the height of the line profiles and enlarged atomic force microscopy (AFM) images of PCFP, ANCFP, and ACFP. Figure 2d–f shows that ANCFP exhibited a relatively bumpy surface, as compared to PCFP and ACFP. The height of the AFM line profiles clearly demonstrates that the ANCFP surface was rougher than that of PCFP and ACFP (Figure S3, Supporting Information). Moreover, nano-sized particles,  $\approx 50$ –200 nm, were distributed over the entire CF surface. The surface roughness of the ANCFP was  $7.2 \pm 0.5$  nm, which was  $\approx 4.2$  and 2 times larger than that of PCFP ( $1.7 \pm 0.1$  nm) and ACFP ( $3.7 \pm 0.4$  nm), respectively. Considering that a small weight change was observed in the thermogravimetric analysis (TGA) thermogram up to 800 °C of the pristine CFs (Figure S4, Supporting Information), it is suggested that the morphological change is related to the carbonized binders. Thus, the function of the PAA and Na-CMC binders before and after carbonization was comprehensively investigated. TGA was used to confirm the thermal behavior of PAA and Na-CMC under an inert atmosphere (Figure 2g). In the PAA and Na-CMC thermograms, a significant weight loss occurred at 50–500 °C, which was attributed to decomposition steps corresponding to the evaporation of moisture, dehydration, and degradation of the polymer.<sup>[46,47]</sup> PAA and Na-CMC still remained after 800 °C, and their remaining weights were 15.0 and 33.0 wt%, respectively, indicating that the PAA and Na-CMC binders were transformed into carbon residues by the thermal treatment. The TGA thermogram of PCFP shows that its weight loss was  $\approx 19$  wt% owing to the partial decomposition and carbonization of binders, resulting in morphological changes on the CF surface.

To verify the carbonization of the binders, each binder was heated up to 800 °C under an inert atmosphere at a ramping rate of 10 °C min<sup>-1</sup>, and structural analyses were performed using X-ray diffraction (XRD) and Raman spectroscopy. After carbonization of PAA and Na-CMC, a broad peak of the (002) plane appeared at  $\approx 26^\circ$ , as shown in Figure 2h, corresponding to the typical interlayer distance in carbon materials. Additionally, the D and G peaks of the PAA and Na-CMC powders after carbonization appeared in the Raman spectra at 1345 and 1584 cm<sup>-2</sup>, respectively (Figure S5, Supporting Information). These results indicate that the polymer chains in PAA and Na-CMC were rearranged into a carbon structure. However, due to carbonization at a low temperature, the carbonized binders revealed an amorphous carbon structure (Figures S5 and S6, Supporting Information). Moreover, the sharp peaks of the carbonized Na-CMC in XRD diffractograms and Raman spectra (Figure 2h and Figure S5, Supporting Information) corresponded to Na<sub>2</sub>CO<sub>3</sub> (JCPDS: 18–1208). However, the XRD diffractogram of ANCFP was analogous to those of PCFP and ACFP because the quantity of binders remaining on the CF surface after carbonization was too small to be analyzed

(Figure S7, Supporting Information). To further investigate the transformation of the binders into amorphous carbon and Na<sub>2</sub>CO<sub>3</sub> by low-temperature carbonization, chemical structure analyses were performed as shown in Figure 2i,j. The oxygen-containing bonds on PCFP were observed in the C1s spectrum (Figure 2i) due to the nature of PAA and Na-CMC. The oxygen functional groups of ANCFP decreased, as compared to that of the PCFP, which is related to the transformation of binders into a carbon structure by the heat treatment. It was additionally confirmed that the peak intensity at 1071.8 eV was distinct in the Na1s spectrum of ANCFP and that a new peak for the CO<sub>3</sub> bond in ANCFP appeared at 531.5 eV (Figure S8, Supporting Information), which was assigned to Na<sub>2</sub>CO<sub>3</sub>.<sup>[48]</sup> Even though ANCFP was washed using DI water to remove Na<sub>2</sub>CO<sub>3</sub>, the oxygen atomic ratio of ACFP (18.14%) was higher than that of pristine CF (11.80%), as shown in Table S1 (Supporting Information), indicating that the remaining oxygen functional groups on ANCFP originated from the amorphous carbon. Therefore, it was demonstrated that the morphological, structural, and chemical modifications on the CF surface occurred by the transformation of binders into amorphous carbon and Na<sub>2</sub>CO<sub>3</sub>.

## 2.2. Electrochemical Performance in a Half Cell

To investigate the effect of the oxygen-containing amorphous carbon and Na<sub>2</sub>CO<sub>3</sub> nanoparticles formed on the CF surface on the electrochemical Li deposition and stripping behavior, galvanostatic charge–discharge tests were performed after pre-cycling for five cycles. In particular, the nucleation overpotential, the difference between the lowest voltage drop and plateau voltage region, can be used to evaluate the degree of lithiophilicity on the electrode surface.<sup>[32,49]</sup> As shown in Figure 3a,b, the initial Li nucleation overpotentials of the PCFP, ACFP, and ANCFP electrodes were 186, 40, and 34 mV, respectively. Interestingly, the electrode comprised of oxygen-containing amorphous carbon showed a significantly lower Li nucleation overpotential than that of the PCFP electrode. Furthermore, the fluctuation in voltage of the PCFP electrode was particularly more extreme than that of the other electrodes during Li electroplating. Additionally, the charge transfer resistance ( $R_{ct}$ ) of ACFP (28.2  $\Omega$ ) and ANCFP (25.6  $\Omega$ ) was similar, but lower than that of PCFP (34.8  $\Omega$ ) in electrochemical impedance spectroscopy (EIS) results (Figure S9b, Supporting Information). This implies that the construction of oxygen-containing amorphous carbon on the CF surface contributes to facilitating uniform Li nucleation. Moreover, as expected, the CEs of the PCFP electrode were inferior to those of the other electrodes in the CE tests at the current densities of 1, 2, and 4 mA cm<sup>-2</sup> with an area capacity of 1 mAh cm<sup>-2</sup> (Figure 3c). In contrast, the ACFP and ANCFP electrodes employing oxygen-containing amorphous carbon exhibited the best cycling stabilities at 1 and 2 mA cm<sup>-2</sup>, respectively. Although the CE of the ACFP electrode started to diminish rapidly after 60 cycles at 4 mA cm<sup>-2</sup>, the ANCFP electrode with Na<sub>2</sub>CO<sub>3</sub> nanoparticles exhibited no drop over 100 cycles (average CE was 97.3%). The CEs of PCFP, ANCFP, and ACFP electrodes with a current density of 4 mA cm<sup>-2</sup> at 100 cycles

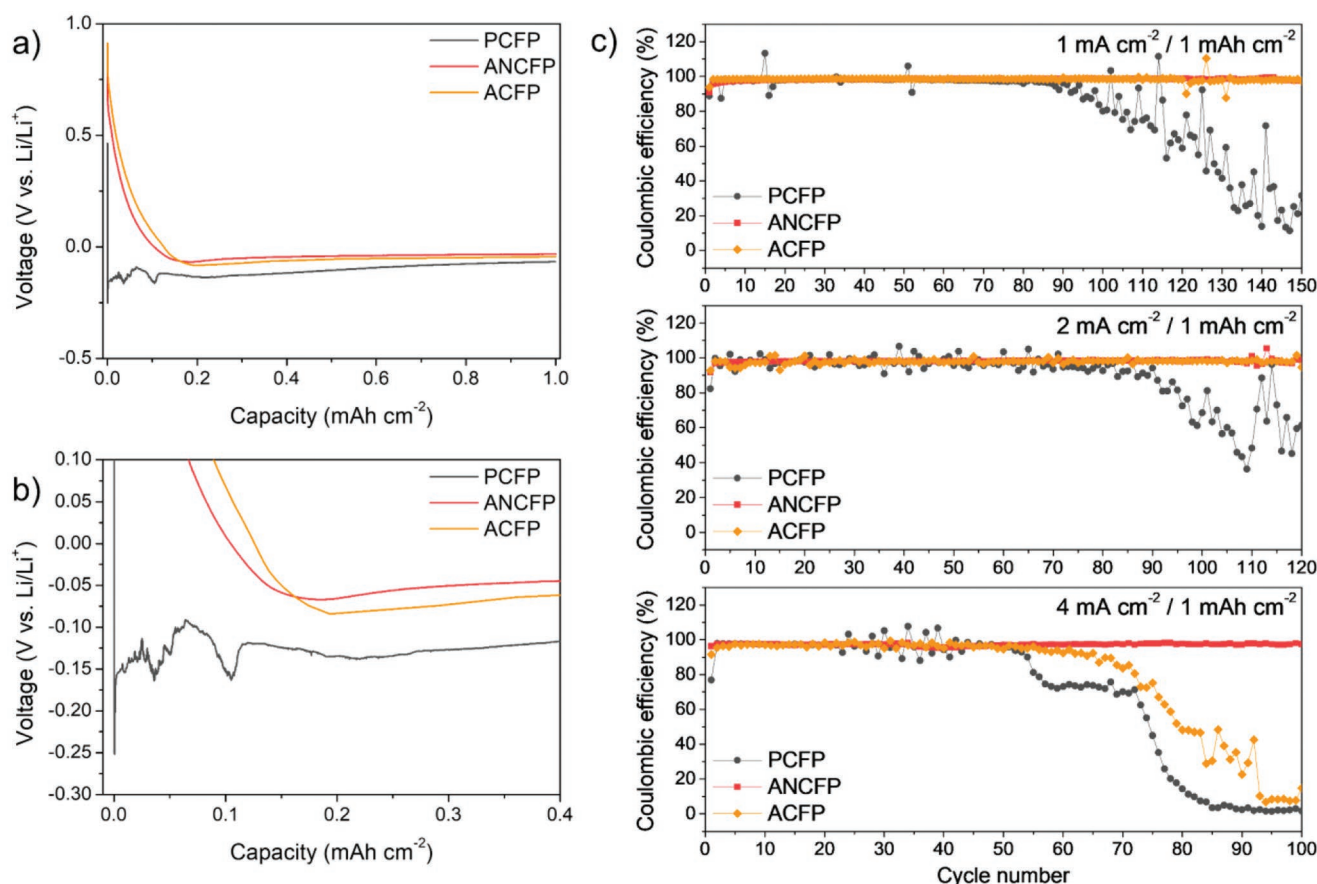


**Figure 3.** a) First discharge profiles of the electrodes and b) magnified discharge profiles of PCFP, ANCFP, and ACFP at a current density of 1 mA cm<sup>-2</sup> for 1 h. c) Comparison of CE tests for the PCFP, ANCFP, and ACFP electrodes at different current densities of 1, 2, and 4 mA cm<sup>-2</sup> with a fixed capacity of 1 mAh cm<sup>-2</sup>.

were 1.7%, 96.7%, and 10.9%, respectively (Figure S10, Supporting Information). Note that the value for a bare Cu foil was 15.9%. We speculate that this is because the sodium additive, one of the representative inorganic ingredients, effectively reduces the irreversible capacity during the initial cycles by forming a dense and compact SEI layer, according to previous studies.<sup>[45,50]</sup> Moreover, Na<sub>2</sub>CO<sub>3</sub> is believed to be the best alkaline carbonate for forming high-quality SEIs to enhance the electrochemical reversibility.<sup>[43,45]</sup>

### 2.3. Morphological Behavior of Li Electroplating on CFPs

To explore the morphological alternation with an increasing amount of Li electroplating, electrochemical Li plating was prepared on the PCFP, ACFP, and ANCFP electrodes by conducting Li electroplating at 0.5, 1, and 2 mAh cm<sup>-2</sup> at a current density of 1 mA cm<sup>-2</sup>. After rinsing the electrodes using 1,2-dimethoxyethane (DME) solvent, the morphological behaviors were analyzed using scanning electron microscopy (SEM). When the Li electroplating was conducted at 0.5 mAh cm<sup>-2</sup>, the PCFP electrode exhibited randomly formed Li deposits and an agglomerated morphology (Figure 4a). When the electroplating was increased to 1 and 2 mAh cm<sup>-2</sup> (Figure 4b,c), Li

dendrites grew locally and significantly on the agglomerated Li. In contrast, Li particles were uniformly plated on the ACFP and ANCFP surfaces, as shown in Figure 4d,g, respectively, due to the lithiophilic property of the amorphous carbon with oxygen functional groups that was uniformly spread on the CF surface. However, Li plating at 1 mAh cm<sup>-2</sup> randomly generated Li dendrites on ACFP, and significant Li dendrite growth was observed at 2 mAh cm<sup>-2</sup>, as shown in Figure 4e,f, respectively. Notably, the morphological alternation on the ANCFP surface by Li electroplating was clearly different from that of the other samples. In particular, at 1 mAh cm<sup>-2</sup> of Li plating, the ANCFP exhibited planar growth of Li deposits on the CF surface and the suppressed growth of dendrites (Figure 4h). Increasing the electroplating to 2 mAh cm<sup>-2</sup> resulted in the planar accumulation of Li deposits on the CF surface, and the CF thickened to 8.6 μm without the formation of problematic Li dendrites (Figure 4i). To further understand the Li dendrites which grow uniformly on the CF surface, the components and resistances of the SEI layer on the electrode were analyzed by X-ray photoelectron spectroscopy (XPS) and EIS after pre-cycling and 50 cycles (fully Li-stripped) with 1 mAh cm<sup>-2</sup> at 1 mA cm<sup>-2</sup>. Figure S11a (Supporting Information) confirms that the SEI layer of all electrodes after pre-cycling consisted of diverse organic and inorganic compounds. Interestingly, the

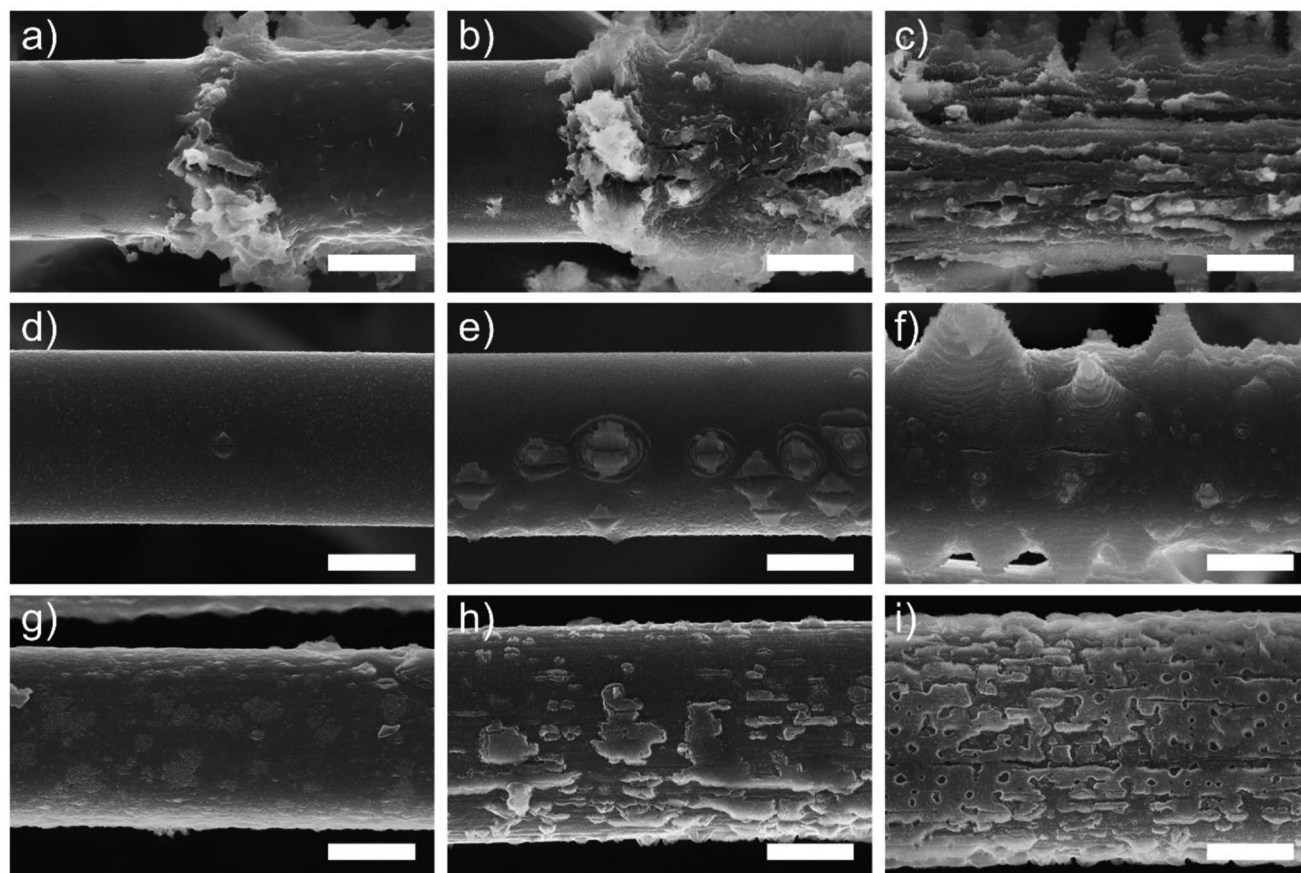


**Figure 4.** SEM micrographs of the a–c) PCFP, d–f) ACFP, and g–i) ANCFP electrodes after Li electrodeposition at 0.5 (a, d, g), 1 (b, e, h), and 2 mA cm<sup>−2</sup> (c, f, i) under a current density of 1 mA cm<sup>−2</sup> (scale bar is 3 μm).

lithium fluoride (LiF) peak for ANCFP, as compared to that for the other samples, was significant, as shown in Figure S12 (Supporting Information), and its intensity was well maintained after 50 cycles. Furthermore, as shown in the XPS C1s in Figure S11b (Supporting Information), only ANCFP showed a prominent peak for lithium carbonate (Li<sub>2</sub>CO<sub>3</sub>), which is a representative inorganic SEI species having excellent mechanical strength and high Li-ion kinetics.<sup>[38,51–53]</sup> In the Nyquist plots (Figure S9, Supporting Information), the ANCFP electrode (34.7 Ω) showed the lowest SEI layer resistance ( $R_{SEI}$ ), as compared to the PCFP (66.5 Ω) and ACFP (43.9 Ω) electrodes after 50 cycles of Li electroplating/stripping. Even though further research is required to elucidate why Na<sub>2</sub>CO<sub>3</sub> induces the formation of an inorganic-rich SEI layer, it is likely that Na cations (Na<sup>+</sup>) on the CF surface attract TFSI<sup>−</sup> anions from the electrolyte and participate in the formation of the SEI layer during pre-cycling. Hence, it is suggested that the abundant inorganic components, such as LiF and Li<sub>2</sub>CO<sub>3</sub>, with high mechanical properties and the low film resistance of the formed SEI, which were confirmed by the XPS and EIS results, alleviate the growth of Li dendrites.<sup>[7,38,51]</sup> This is further supported by the bulk moduli of LiF (45.5–89.4 GPa) and Li<sub>2</sub>CO<sub>3</sub> (43.1–50.5 GPa), which are known to be sufficient to reduce the SEI layer to prevent the incidence of Li dendrites (modulus of 2.7–21 GPa) and tearing of the SEI layer.<sup>[54,55]</sup>

#### 2.4. Feasibility Study on Li Infusion Process and Practical Full Cell LMBs

Among the methods to manufacture practical LMAs, the Li infusion process is a more preferable and affordable method than electroplating because it is a shorter process.<sup>[56,57]</sup> Therefore, the infusion process was adopted for loading Li into the CFPs (the detailed procedure is described in the Experimental section). **Figure 5a** and Video S1 (Supporting Information) show that the molten Li infused into the ANCFP electrode within a few seconds, suggesting that the greatly enhanced wettability of molten Li was accomplished by modulating the CF with a bumpy surface.<sup>[58]</sup> The weight of the Li infused into ANCFP was up to 23.4 mg cm<sup>−2</sup>. Although ACFP also exhibited the Li infusion behavior, a longer time of 4 min was required to complete the process (Video S2, Supporting Information). Lithium infusion did not occur in the PCFP electrode at all (Video S3, Supporting Information). To further confirm the cycling stability of the as-prepared LMAs at various current densities, symmetrical cells, configured with Li-infused ANCFP (Li@ANCFP) and bare Li electrodes, with a fixed capacity of 1 mAh cm<sup>−2</sup> were prepared as shown in Figure 5b. At a current density of 1 mA cm<sup>−2</sup>, the Li@ANCFP symmetrical cell exhibited a small voltage hysteresis (sum of the overpotential at the Li electroplating and stripping states) of 24 mV



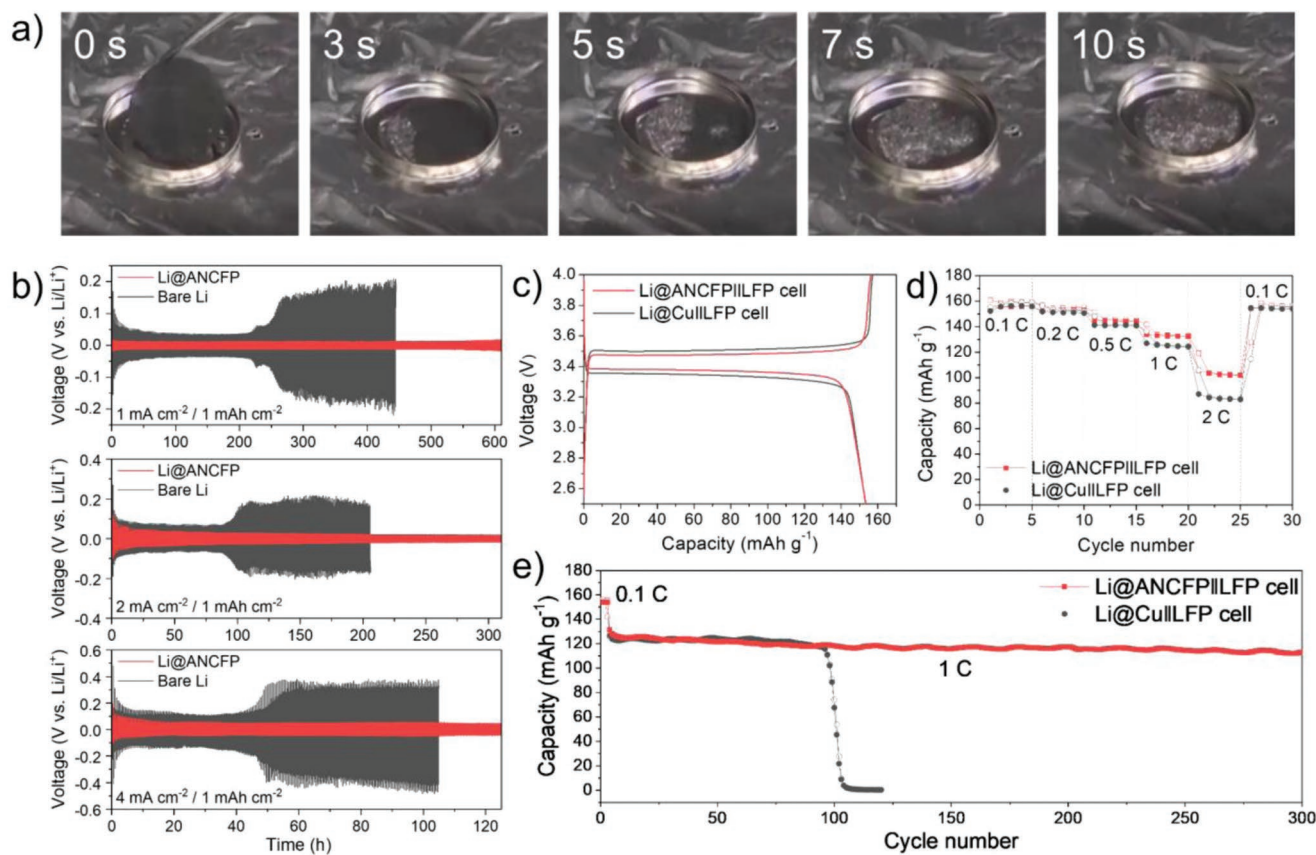


**Figure 5.** a) Optical micrographs of the Li infusion into the ANCFP electrode within 10 s. b) Cycling stabilities of the bare Li and Li@ANCFP electrodes in symmetric cells at different current densities of 1, 2, and 4 mA cm<sup>-2</sup> with a fixed capacity of 1 mAh cm<sup>-2</sup>. c) Galvanostatic charge–discharge curves (at 0.1 C), d) rate capability, and e) cycling stability (at 1 C) of the Li@Cu||LFP and Li@ANCFP||LFP full-cells.

and stable voltage profiles for 600 h, whereas the overpotential of the bare Li cell increased from 70 mV after 50 cycles to 280 mV after 150 cycles. When the current densities were 2 and 4 mA cm<sup>-2</sup>, the cycling stabilities of the Li@ANCFP symmetrical cell were maintained even after 300 cycles, indicating that polarization reduction and Li dendrite suppression can be achieved using oxygen-containing amorphous carbon and an inorganic-rich SEI layer on the CF surface. However, the degradation of stability and drastic growth of the overpotential of the bare Li symmetrical cell continued to accelerate over a short period of time, especially when the current densities increased. Moreover, as shown in Figures S13–S15 (Supporting Information), the bare Li cells exhibited fluctuations in voltage after 150 cycles, which is evidence of the repeated formation of dead Li and an SEI layer due to the growth of Li dendrites.<sup>[59,60]</sup>

LMB full-cells were assembled by pairing Li@Cu and Li@ANCFP with a lithium iron phosphate (LFP) cathode ( $\approx 13$  mg cm<sup>-2</sup>) to conduct a feasibility study of the ANCFP for a practical anode framework. The Li@ANCFP anodes were prepared using Li electroplating with a capacity of 6 mAh cm<sup>-2</sup> at 1 mA cm<sup>-2</sup> to precisely quantify an  $\approx 3.0$  capacity ratio of negative to positive electrodes (N/P ratio). Figure 5c shows a comparison of the polarization of Li@ANCFP and Cu/Li at 0.1 C. The polarization of the Li@ANCFP||LFP cell was 110 mV

at 0.1 C (1 C = 170 mA g<sup>-1</sup>), which was lower than that of the Li@Cu||LFP cell (180 mV). At various current densities of 0.2, 0.5, and 1 C (Figure S16, Supporting Information), the voltage profiles demonstrated reduced polarization after employing the Li@ANCFP electrode. Although there were no significant differences between the capacities of the Li@ANCFP||LFP and Li@Cu||LFP cells at low current densities (0.1, 0.2, 0.5, and 1 C), the Li@ANCFP||LFP cell achieved a higher capacity (101 mAh g<sup>-1</sup>) than the Li@Cu||LFP cell (83 mAh g<sup>-1</sup>) at a high current density of 2.0 C (Figure 5d), meaning that 3D ANCFP enhances the kinetics of Li-ion deposition.<sup>[61,62]</sup> Furthermore, the cycling stability test performed at 1.0 C (Figure 5e) demonstrated that the Li@Cu||LFP cell exhibited a rapid decline after 100 cycles, whereas the Li@ANCFP||LFP cell showed excellent cycling stability with a capacity retention of 85% over 300 cycles. This indicates that the Li plating and stripping processes on ANCFP were stable and reversible without the formation of problematic Li dendrites. A hierarchical surface was simply designed and fabricated on the CF using carbonizing binders, and an adequate electrochemical performance was attained, as compared to the half and symmetrical cells in the literature (Table S2, Supporting Information). Furthermore, it was notable that an outstanding long-term stability was achieved despite the practical loading of the cathode in the full-cell. Additionally, our approach realizes the fabrication of significantly

lighter LMA (Li@ANCFP anode (3 mg cm<sup>-2</sup>)) than the present LMA of Li@Cu anode (15.3 mg cm<sup>-2</sup>), and moreover, a high specific energy of 428 Wh kg<sup>-1</sup> as a Li@ANCFP||LFP full-cell (Table S3, Supporting Information).

### 3. Conclusions

This study demonstrated a new methodology to provide CF-based 3D free-standing LMAs for batteries with high-energy density. Chopped CFs and two polymer binders were used to prepare CF paper using the wet-laid process. The resultant material was heat-treated at 800 °C. Hence, a surface-modulated CFP, containing amorphous carbon with oxygen-related functional groups and Na<sub>2</sub>CO<sub>3</sub> nanoparticles, was obtained. The ANCFP, as a 3D framework, was utilized as an LMA after Li was infused or electroplated into the CFP. Subsequently, the mechanism for how Li-incorporated CFPs effectively perform electrochemical work in half and full-cells to mimic LMB was investigated. Because of the oxygen-containing amorphous carbon on the CF surface, the modified ANCFP electrode exhibited a lower Li nucleation overpotential (34 mV) than that of the control sample of a pure CFP electrode (186 mV). Furthermore, Li nucleation occurred on the surface and Li continuously covered the CFs without the formation of Li dendrites because of the inorganic component-rich SEI layer. Consequently, CE of ~97% were achieved during Li plating/stripping in the half cell. In the symmetrical cells, the Li@ANCFP||Li@ANCFP also exhibited excellent cycling stability and a steady overpotential at various current densities of 1, 2, and 4 mA cm<sup>-2</sup> for 300 cycles. An electrochemical long-term stability was also verified in the practical full-cell with a LFP cathode with a high loading of 13 mg cm<sup>-2</sup>. The Li@ANCFP||LFP full-cell maintained a capacity of 85% at 1 C after 300 cycles. Moreover, the Li@ANCFP anode exhibited a high-energy density of 428 Wh kg<sup>-1</sup>, resulting from its ~fivefold lighter weight, as compared to the Li@Cu anode. Therefore, we believe that our advanced strategy, which is different to previously reported technologies, such as adding novel and toxic additives in electrolytes and surface morphology modification using complicated methods, will enable the realization of a highly stable LMA with outstanding electrochemical performance for application in the practical energy storage fields to replace conventional LiBs.

### 4. Experimental Section

**Preparation of ANCFP:** CFP was fabricated by the filtering method which was reported in a previous study.<sup>[63]</sup> In detail, 6 mm-long chopped CFs (T700 grade, Toray Industries, Inc.) were washed using a sonicator for 90 min in acetone (Dejung Chemicals) to remove the sizing agents and impurities on the CF surfaces. Na-CMC (12 g, Mw = 90000, Sigma-Aldrich) and PAA (2 g, Mw = 450000, Sigma-Aldrich) were completely dissolved in deionized water (2000 mL) by stirring. The chopped CFs (0.65 g) were added to the solution (binders dissolved in DI water), and the mixture was stirred for 2 h. After the CFs were sufficiently dispersed in the solution, the mixture was filtered using a spun bond filter and aspirator pump. The PCFP was obtained after the water was removed by drying the filtrate in a vacuum oven at 90 °C. To prepare the ANCFP sample, PCFP was carbonized at 800 °C in an inert atmosphere

at a heating rate of 10 °C min<sup>-1</sup>. The weight and thickness of ANCFP were 1.0 ± 0.2 mg cm<sup>-2</sup> and 120 ± 20 μm, respectively. Additionally, the Na<sub>2</sub>CO<sub>3</sub> on the ANCFP surface was sufficiently washed with DI water to obtain ACFP.

**Characterization:** SEM (Nova NanoSEM 450) and AFM were used to determine the morphologies of the samples. After the AFM images were obtained using an NX10 with a PPP-NCHR noncontact cantilever (tip radius: <10 nm, Park Systems), the roughness of the sample was estimated using the Nanoscope analysis software. To verify the thermal behavior of the binders, TGA (TA Instruments SDT 2960) was performed at a heating rate of 10 °C min<sup>-1</sup> up to 800 °C in an inert atmosphere. The carbon structure was confirmed using XRD (Rigaku Smart Lab) with a Cu Kα source at a scan rate of 5° min<sup>-1</sup>. Raman spectroscopy (Renishaw) with an Ar-ion laser (λ = 514 nm) was used to determine the degree of disorder in the carbon structure. The surface chemical composition was investigated using XPS (Multilab 2000, Thermo Fisher) with an Al Kα (1486.6 eV) X-ray source on a 200 μm<sup>2</sup> point area.

**Electrochemical Measurements:** To analyze the electrochemical characteristics of the samples, 2032-type coin cells were assembled in an Ar filled glove box with O<sub>2</sub> and H<sub>2</sub>O contents < 1 ppm. 1 M Bis(trifluoromethane)sulfonimide (LiTFSI) in 1,3-dioxolane (DOL) and DME (vol. 1:1) with 2 wt% lithium nitrate (LiNO<sub>3</sub>) as the electrolyte was used in all the coin cells. The amount of electrolyte used in all coin cells was 60 μL. The prepared sample, Li metal, and Celgard 2400 were used as a working electrode, counter electrode, and separator, respectively. To test the CE of the electrode, the electrochemical performance of the coin cells was measured at different current densities of 1, 2, and 4 mA cm<sup>-2</sup> for 1 mAh cm<sup>-2</sup> after pre-cycling for 5 cycles in the voltage range of 0–1 V with 0.1 mA cm<sup>-2</sup>. The coin cells were disassembled after Li electroplating at 0.5, 1.0, and 2.0 mAh cm<sup>-2</sup> at 1 mA cm<sup>-2</sup> and then SEM analysis was performed to investigate the morphologies of Li plating. To infuse Li in PCFP, ACFP, and ANCFP, metallic Li was first melted on a hotplate at 300 °C in an Ar-filled glove box, and then the as-prepared electrode was dipped into the molten Li until the electrode was completely covered. Additionally, symmetric cells were assembled using two identical Li metals and Li@ANCFP. EIS was performed using an electrochemical potentiostat (Autolab PGSTAT302/NAutolab FRA2) at frequencies of 0.01–100 kHz with an amplitude of 5 mV. The electrochemical resistances were obtained from the Nyquist plots based on the equivalent circuit (inset of Figure S9b, Supporting Information). The cathode for the full-cell test was prepared using LFP (MTI Korea), Super P (Alfa Aesar), and polyvinylidene fluoride (PVdF, Sigma-Aldrich) as an active material, conductive agent, and binder, respectively. The LFP, Super P, and PVdF were mixed to an 8:1:1 weight ratio in N-methyl-2-pyrrolidone (NMP, Deajung chemicals) solvent, and then the slurry was coated on foil. Subsequently, the slurry was dried in a vacuum oven at 80 °C for 12 h. The weight and thickness of the LFP cathode was 13.2 ± 0.6 mg cm<sup>-2</sup> and 108 ± 5 μm, respectively. To configure the ~3 N/P ratio for the full-cell, the Li@ANCFP anode was prepared using Li electroplating with a capacity of 6 mAh cm<sup>-2</sup> at 1 mA cm<sup>-2</sup>. A commercial Li@Cu (15.3 mg cm<sup>-2</sup>) anode was used to compare the full-cell performance. The full-cell was composed of an LFP cathode, separator, and Li@ANCFP or Li@Cu anodes.

The energy density of the full-cells was calculated based on the weight of the cathode and anode materials (Table S3, Supporting Information) using Equation (1):

$$\text{Energy density (Wh kg}^{-1}\text{)} = \frac{C_{\text{cell}} (\text{Ah}) \times V_a (\text{V})}{W_{\text{a+c}} (\text{kg})} \quad (1)$$

where  $C_{\text{cell}}$  is the capacity of the cell,  $V_a$  is the average voltage, and  $W_{\text{a+c}}$  is the weight of the anode and cathode materials.

### Supporting Information

Supporting Information is available from the Wiley Online Library or from the author.



## Acknowledgements

This study was supported by a grant from the Korean Institute of Science and Technology (KIST) Institutional Program (2E32633), the National R&D Program through the National Research Foundation of Korea (NRF) funded by the Ministry of Science and ICT (2021M3H4A1A03041296), and the Korea government (NRF-2021R1A2C1009947), Republic of Korea.

## Conflict of Interest

The authors declare no conflict of interest.

## Data Availability Statement

The data that support the findings of this study are available from the corresponding author upon reasonable request.

## Keywords

3D free-standing, carbon fiber electrodes, hierarchical surfaces, lithium metal anodes

Received: November 7, 2022

Revised: December 18, 2022

Published online:

- [1] M. H. Eric, R. M. Ali, A. Y. Ku, K. Alissa, H. Gavin, H. Oliver, *Science* **2021**, 373, 384.
- [2] H. Yuan, X. Ding, T. Liu, J. Nai, Y. Wang, Y. Liu, C. Liu, X. Tao, *Mater. Today* **2022**, 53, 173.
- [3] S. Li, J. Huang, Y. Cui, S. Liu, Z. Chen, W. Huang, C. Li, R. Liu, R. Fu, D. Wu, *Nat. Nanotechnol.* **2022**, 17, 613.
- [4] D. Lin, Y. Liu, Y. Cui, *Nat. Nanotechnol.* **2017**, 12, 194.
- [5] P. Albertus, S. Babinec, S. Litzelman, A. Newman, *Nat. Energy* **2018**, 3, 16.
- [6] J. Wang, Q. Ma, S. Sun, K. Yang, Q. Cai, E. Olsson, X. Chen, Z. Wang, A. M. Abdelkader, Y. Li, W. Yan, S. Ding, K. Xi, *eScience* **2022**, 2, 655.
- [7] F. Wu, Y.-X. Yuan, X.-B. Cheng, Y. Bai, Y. Li, C. Wu, Q. Zhang, *Energy Storage Mater.* **2018**, 15, 148.
- [8] J. H. Um, K. Kim, J. Park, Y.-E. Sung, S.-H. Yu, *J. Mater. Chem. A* **2020**, 8, 13874.
- [9] J.-F. Ding, R. Xu, X.-X. Ma, Y. Xiao, Y.-X. Yao, C. Yan, J.-Q. Huang, *Angew. Chem., Int. Ed.* **2022**, 61, e202115602.
- [10] H. J. S. Sand, *London, Edinburgh, Dublin Philos. Mag. J. Sci.* **1901**, 1, 45.
- [11] C. Brissot, M. Rosso, J.-N. Chazalviel, S. Lascaud, *J. Power Sources* **1999**, 81–82, 925.
- [12] M. Jäckle, A. Groß, *J. Chem. Phys.* **2014**, 141, 174710.
- [13] X. Sun, X. Zhang, Q. Ma, X. Guan, W. Wang, J. Luo, *Angew. Chem., Int. Ed.* **2020**, 59, 6665.
- [14] S. Chen, Y. Xiang, G. Zheng, Y. Liao, F. Ren, Y. Zheng, H. He, B. Zheng, X. Liu, N. Xu, M. Luo, J. Zheng, Y. Yang, *ACS Appl. Mater. Interfaces* **2020**, 12, 27794.
- [15] F. Yongjin, Z. S. Lin, W. Zhi-Peng, L. Deyan, L. X. Wen, *Sci. Adv.* **2021**, 7, 3626.
- [16] Z. Lyu, G. J. H. Lim, R. Guo, Z. Pan, X. Zhang, H. Zhang, Z. He, S. Adams, W. Chen, J. Ding, J. Wang, *Energy Storage Mater.* **2020**, 24, 336.
- [17] J. Qian, W. A. Henderson, W. Xu, P. Bhattacharya, M. Engelhard, O. Borodin, J.-G. Zhang, *Nat. Commun.* **2015**, 6, 6362.
- [18] T. Jiang, P. He, G. Wang, Y. Shen, C.-W. Nan, L.-Z. Fan, *Adv. Energy Mater.* **2020**, 10, 1903376.
- [19] J. Cao, Y. Xie, W. Li, X. Wang, Y. Yang, Q. Zhang, J. Guo, C. Yang, S. Cheng, C. Zhang, K. Wang, *Mater. Today Energy* **2021**, 20, 100663.
- [20] A.-L. Chen, N. Shang, Y. Ouyang, L. Mo, C. Zhou, W. W. Tjiu, F. Lai, Y.-E. Miao, T. Liu, *eScience* **2022**, 2, 192.
- [21] X. Li, H. Jiang, Y. Liu, X. Guo, G. He, Z. Chu, G. Yu, *EcoMat* **2022**, 4, e12162.
- [22] C. Guo, Y. Guo, R. Tao, X. Liao, K. Du, H. Zou, W. Zhang, J. Liang, D. Wang, X.-G. Sun, S.-Y. Lu, *Nano Energy* **2022**, 96, 107121.
- [23] P. Qing, Z. Wu, Y. Chen, F. Tang, H. Yang, L. Chen, *J. Energy Chem.* **2022**, 72, 149.
- [24] J. Wang, H. Liu, H. Wu, Q. Li, Y. Zhang, S. Fan, J. Wang, *Carbon* **2021**, 177, 181.
- [25] T. Foroozan, F. A. Soto, V. Yurkiv, S. Sharifi-Asl, R. Deivanayagam, Z. Huang, R. Rojaee, F. Mashayek, P. B. Balbuena, R. Shahbazian-Yassar, *Adv. Funct. Mater.* **2018**, 28, 1705917.
- [26] H. Cheng, S. Zhang, J. Mei, L. Qiu, P. Zhang, X. Xu, J. Tu, J. Xie, X. Zhao, *Sustainable Energy Fuels* **2020**, 4, 5773.
- [27] H. Gan, J. Wu, H. Chen, R. Li, H. Liu, *J. Mater. Chem. A* **2020**, 8, 13480.
- [28] C. Lu, M. Tian, X. Zheng, C. Wei, M. H. Rummeli, P. Strasser, *R. Yang, Chem. Eng. J.* **2022**, 430, 132722.
- [29] H. Liu, J. Di, P. Wang, R. Gao, H. Tian, P. Ren, Q. Yuan, W. Huang, R. Liu, Q. Liu, M. Feng, *Carbon Energy* **2022**, 4, 654.
- [30] X.-X. Ma, X. Chen, Y.-K. Bai, X. Shen, R. Zhang, Q. Zhang, *Small* **2021**, 17, 2007142.
- [31] C. Xiang, C. Xiao-Ru, H. Ting-Zheng, L. Bo-Quan, C. Xin-Bing, Z. Rui, Z. Qiang, *Sci. Adv.* **2019**, 5, 7728.
- [32] R. Zhang, X.-R. Chen, X. Chen, X.-B. Cheng, X.-Q. Zhang, C. Yan, Q. Zhang, *Angew. Chem., Int. Ed.* **2017**, 56, 7764.
- [33] C. Zhao, X. Yin, Z. Guo, D. Zhao, G. Yang, A. Chen, L. Fan, Y. Zhang, N. Zhang, *Chin. Chem. Lett.* **2021**, 32, 2254.
- [34] G. Huang, J. Han, F. Zhang, Z. Wang, H. Kashani, K. Watanabe, M. Chen, *Adv. Mater.* **2019**, 31, 1805334.
- [35] Y. Liu, X. Qin, S. Zhang, Y. Huang, F. Kang, G. Chen, B. Li, *Energy Storage Mater.* **2019**, 18, 320.
- [36] W. Liu, Y. Xia, W. Wang, Y. Wang, J. Jin, Y. Chen, E. Paek, D. Mitlin, *Adv. Energy Mater.* **2019**, 9, 1802918.
- [37] J. Zhu, P. Li, X. Chen, D. Legut, Y. Fan, R. Zhang, Y. Lu, X. Cheng, Q. Zhang, *Energy Storage Mater.* **2019**, 16, 426.
- [38] Z. Han, C. Zhang, Q. Lin, Y. Zhang, Y. Deng, J. Han, D. Wu, F. Kang, Q.-H. Yang, W. Lv, *Small Methods* **2021**, 5, 2001035.
- [39] P. Zhai, L. Liu, X. Gu, T. Wang, Y. Gong, *Adv. Energy Mater.* **2020**, 10, 2001257.
- [40] M. Wu, Y. Li, X. Liu, S. Yang, J. Ma, S. Dou, *SmartMat* **2021**, 2, 5.
- [41] H. Wang, Y. Shao, S. Mei, Y. Lu, M. Zhang, J. Sun, K. Matyjaszewski, M. Antonietti, J. Yuan, *Chem. Rev.* **2020**, 120, 9363.
- [42] J. Liu, H. Yuan, X. Tao, Y. Liang, S. J. Yang, J.-Q. Huang, T.-Q. Yuan, M.-M. Titirici, Q. Zhang, *EcoMat* **2020**, 2, e12019.
- [43] Y. Zhang, Y. Gui, X. Wu, H. Feng, L. Wang, A. Zhang, X. Li, T. Xia, L. Zhang, P. Zhang, C. Zhang, *Electrochem. Solid-State Lett.* **2009**, 12, A120.
- [44] S. Komaba, M. Watanabe, H. Groult, N. Kumagai, K. Okahara, *Electrochem. Solid-State Lett.* **2006**, 9, A130.
- [45] S. Komaba, M. Watanabe, H. Groult, N. Kumagai, *Carbon* **2008**, 46, 1184.
- [46] V. Datsyuk, L. Billon, C. Guerret-Piécourt, S. Dagréou, N. Passade-Boupatt, S. Bourrigaud, O. Guerret, L. Couvreur, *J. Nanomater.* **2007**, 2007, 74769.
- [47] A. A. Ibrahim, A. M. Adel, Z. H. A. El-Wahab, M. T. Al-Shemy, *Carbohydr. Polym.* **2011**, 83, 94.
- [48] K. Dideriksen, C. Frandsen, N. Bovet, A. F. Wallace, O. Sel, T. Arbour, A. Navrotsky, J. J. De Yoreo, J. F. Banfield, *Geochim. Cosmochim. Acta* **2015**, 164, 94.

- [49] P. Biswal, S. Stalin, A. Kludze, S. Choudhury, L. A. Archer, *Nano Lett.* **2019**, *19*, 8191.
- [50] S. Komaba, T. Itabashi, B. Kaplan, H. Groult, N. Kumagai, *Electrochem. Commun.* **2003**, *5*, 962.
- [51] R. Pathak, K. Chen, A. Gurung, K. M. Reza, B. Bahrami, J. Pokharel, A. Baniya, W. He, F. Wu, Y. Zhou, K. Xu, Q. (Quinn) Qiao, *Nat. Commun.* **2020**, *11*, 93.
- [52] Q. Zhang, J. Pan, P. Lu, Z. Liu, M. W. Verbrugge, B. W. Sheldon, Y.-T. Cheng, Y. Qi, X. Xiao, *Nano Lett.* **2016**, *16*, 2011.
- [53] H.-H. Sun, A. Dolocan, J. A. Weeks, R. Rodriguez, A. Heller, C. B. Mullins, *J. Mater. Chem. A* **2019**, *7*, 17782.
- [54] H. Shin, J. Park, S. Han, A. M. Sastry, W. Lu, *J. Power Sources* **2015**, *277*, 169.
- [55] L. Zhang, T. Yang, C. Du, Q. Liu, Y. Tang, J. Zhao, B. Wang, T. Chen, Y. Sun, P. Jia, H. Li, L. Geng, J. Chen, H. Ye, Z. Wang, Y. Li, H. Sun, X. Li, Q. Dai, Y. Tang, Q. Peng, T. Shen, S. Zhang, T. Zhu, J. Huang, *Nat. Nanotechnol.* **2020**, *15*, 94.
- [56] J. Chang, H. Hu, J. Shang, R. Fang, D. Shou, C. Xie, Y. Gao, Y. Yang, Q. N. Zhuang, X. Lu, Y. K. Zhang, F. Li, Z. Zheng, *Small* **2022**, *18*, 2105308.
- [57] A. Kwade, W. Haselrieder, R. Leithoff, A. Modlinger, F. Dietrich, K. Droeder, *Nat. Energy* **2018**, *3*, 290.
- [58] R. Zhang, X. Chen, X. Shen, X.-Q. Zhang, X.-R. Chen, X.-B. Cheng, C. Yan, C.-Z. Zhao, Q. Zhang, *Joule* **2018**, *2*, 764.
- [59] K.-H. Chen, K. N. Wood, E. Kazyak, W. S. LePage, A. L. Davis, A. J. Sanchez, N. P. Dasgupta, *J. Mater. Chem. A* **2017**, *5*, 11671.
- [60] H. Dai, X. Gu, J. Dong, C. Wang, C. Lai, S. Sun, *Nat. Commun.* **2020**, *11*, 643.
- [61] L. Liu, Y.-X. Yin, J.-Y. Li, S.-H. Wang, Y.-G. Guo, L.-J. Wan, *Adv. Mater.* **2018**, *30*, 1706216.
- [62] Y. Wang, H.-Q. Sang, W. Zhang, Y. Qi, R.-X. He, B. Chen, W. Sun, X.-Z. Zhao, D. Fu, Y. Liu, *ACS Appl. Mater. Interfaces* **2020**, *12*, 51563.
- [63] S. Lee, D. Jang, Y. S. Chung, S. Lee, *Composites, Part A* **2020**, *137*, 105992.